Effect of type-III Anti-Freeze Proteins (AFPs) on CO_2 hydrate formation rate

Zhou, Hongxia; Infante Ferreira, Carlos

DOI
10.1016/j.ces.2017.03.060

Publication date
2017

Document Version
Accepted author manuscript

Published in
Chemical Engineering Science

Link to formal publication in Chemical Engineering Science (Elsevier): https://doi.org/10.1016/j.ces.2017.03.060

Effect of type-III Anti-Freeze Proteins (AFPs) on CO_2 hydrate formation rate

Hongxia Zhou, Carlos Infante Ferreira*

Delft University of Technology, Process & Energy Department,

Leeghwaterstraat 39, 2628 CB, Delft, The Netherlands.

ABSTRACT

CO_2 hydrate slurry is a favourable direct coolant of fresh products due to its large latent heat and phase change temperature around 7 °C. Continuous production of this slurry is, however, difficult to realise due to the high rate of hydrate formation. The use of additives is proposed with the purpose of decreasing the formation rate so that the controllability of the process is improved. Type-III Antifreeze Proteins (AFPs) are non-poisonous additives which, at low dosage, have proven to be efficient limiters of gas hydrate formation. The effect of these additives on the CO_2 hydrate formation rate is experimentally investigated in this study.

The concentration of the AFPs investigated in this research is 10 ppm. Experimental results show that the supercooling degree of the solution is only slightly affected by the addition of AFPs. Results also show that the addition of AFPs slows down the dissolution rate of CO_2 gas into the aqueous solution which is the first step of gas hydrate formation. A hydrate growth equation has been used, from which the experimental mass transfer coefficient of CO_2 through the solution has been derived. Results show that the decrease of hydrate growth rate with the addition of AFPs can be related to a decrease of the CO_2 mass transfer coefficient which gives a lower mass transport rate from bulk liquid phase to the crystal interface.

Keywords: CO_2 hydrate; Anti-Freeze Proteins (AFPs); Growth rate; Mass transfer.

Nomenclature

A	Area	m^2	*bath*	Bath
c_p	Specific heat		*b*	Bulk
d	Diameter	m	*c*	Coil
D_c	Coil diameter	m	*crit*	Critical
De	Dean number		*exp*	Experimental
f	Friction factor		*g-l*	Gas to liquid

Corresponding Author: C.A.InfanteFerreira@tudelft.nl; Tel: +31 152784894.

F	Energy loss		*h*	Hydrate
G	Mass growth rate	kg h^{-1}	*i*	Inner
h	Heat transfer coefficient	W m^{-2} K^{-1}	*inlet*	Inlet
i	Enthalpy		*int*	interfacial
k	Mass transfer coefficient	m s^{-1}	*ln*	Logarithmic
K	Kinetic constant	m^3 s^{-1}	l	Liquid
L	Length	m	*loss*	Loss
$\dot{m}$	Mass flow rate	kg s^{-1}	*L*	Local
n	Number of gas molecules	mol	*o*	Outer
Nu	Nusselt number		*outlet*	Outlet
P	Pressure	Pa	*pred*	Predicted
Pr	Prandtl number		*s*	Slurry
$\dot{Q}$	Energy flow	J s^{-1}	sat	Saturated
Re	Reynolds number($=\frac{\rho d \omega}{\mu}$)		*sol*	Solution
T	Temperature	K	*str*	Straight
t	Time	s	*w*	Wall
U	Overall heat transfer coefficient	W m^{-2} K^{-1}	**Abbreviations**	
x	Molar fraction	mol mol^{-1}	AFP	Anti-Freeze Proteins
Greek			KHIs	Kinetic Hydrate Inhibitors
Δ	Difference		LHTS	Latent Heat Thermal Storage
δ	Crystal layer thickness	m	PCM	Phase Change Material
λ	Thermal conductivity	W m^{-1} K^{-1}	PVCap	Polyvinyl Caprolactam
μ	Viscosity	Pa·s	PVP	Polyvinyl Pyrrolidone
ν	Linear growth rate	m s^{-1}	[Py14]-Br	N-butyl-N-methylpyrrolidinium
ρ	Density	kg m^{-3}	THIs	Thermodynamic Hydrate Inhibitors
ω	Velocity	m s^{-1}	THF	Tetrahydrofuran
Subscript			Poly[VP/VC]	N-Vinyl pyrrolidone-co-N-Vinyl caprolactam
av	Average			

1. Introduction

Clathrate hydrates are ice-like compounds and have crystalline structures that are formed with proper combination of small guest molecules, such as methane, ethane, propane, carbon dioxide, and hydrogen-sulfides, which are trapped in cavities of a hydrogen-bonded water framework. There are three main crystallographic structures of hydrates: sI, sII, sH, which differ by the cavity size and shape (Sloan 1998; Ripmeester et al. 1987; Ripmeester and Ratcliffe 1990; Englezos 1993; Khokhar et al. 1998; Jager et al. 1999). The hydrates gained industrial interest when it was found that they form under certain pressure and temperature in oil and gas pipelines and create blockage (Hammerschimidt, 1934). Formation of gas hydrates in oil and gas pipelines and processing equipment is something that the petroleum industry is most concerned about since it can lead to flow blockage and severe economic loss. Clathrate hydrate slurries composed of hydrates flowing in suspension in solutions are recently been proposed as (pumpable) phase change materials (Zhou et al., 2015).

Pumpable phase change materials (PCMs) are one of the most efficient candidates to be applied as a kind of secondary cooling fluids due to the large latent heat when undergoing a phase change from solid to liquid or liquid to gas or vice versa, which can substantially increase the energetic and economic performance of secondary cooling systems. Ice slurries have been introduced as secondary cooling fluids in the beginning of the century (Bel and Lallemand, 1999; Tanino and Kozawa, 2001; Ayel et al., 2003; Matsumoto et al., 2004). These systems show improved performance when compared with single-phase secondary refrigerants (Kauffeld et al., 1999). CO_2 hydrate slurry is a favourable secondary fluid which can be applied in direct contact to fresh products and in air-conditioning systems: it has a large latent heat (387 kJ/kg) which has been measured by Fournaison et al. (2004) using a DTA apparatus and positive phase change temperature (7-8 °C). This allows for the application of primary refrigeration cycles which operate at significantly higher evaporating temperatures than cycles applied in conventional rapid chilling plants. Making use of a latent heat thermal storage system (LHTS), the generation unit runs in a day/night mode, therefore the condensing temperature of the refrigeration cycle can be lowered. In these ways, the refrigeration cycle efficiency is correspondingly significantly improved in comparison with conventional designs.

Sari et al. (2008) have studied the formation of CO_2 hydrate slurry in a double tube heat exchanger. They injected high pressure CO_2 into cooled solution to form hydrate slurry under temperature range 1.5~2°C and pressure about 35 bar. In their case, formation and dissociation are processed alternatively. This low temperature of the hydrate slurry is not beneficial when the slurry is applied in air-conditioning systems. Marinhas et al. (2006) studied CO_2 hydrate slurry flow in tubes. The total volume of their experimental loop is 0.297 L, with flow rate maximum 0.93 m/s. The experimental device is placed in an air-controlled room horizontally. Hydrate dissociation is processed after 2 hours of formation. The experimental condition of their experiments is along the L_w-H-V (aqueous-hydrate-vapor) line. Yang et al. (2011) studied CO_2 hydrate formation in a fin-tube heat exchanger. The diameter of the tube is 8 mm. There are 180° bends in the tube exchanger. The longest stable run has lasted for more than 1 h and was limited by the recirculation of process water. All of the investigations mentioned above have one thing in common, in their apparatus, there is no free space for gas phase, all the gas is dissolved into the solution. Jerbi et al. (2010) studied CO_2 hydrate slurry formation and dissociation in the same apparatus as Marinhas et al. (2006). They did two different types of experiments: 1) open system: firstly cool down water/solution to subcooling, and then inject CO_2 into the subcooled solution to form hydrate (Pre-cooling) and the pressure is maintained by filling CO_2 continuously. 2) closed system: firstly inject CO_2 into water making a CO_2-saturated solution, and then cool down the solution until hydrates are formed (Pre-injection), no extra CO_2 is charged during the process. It's concluded from their experiments that the continuous filling of CO_2 in the open system provides a force for hydrate formation, which results in a larger amount of hydrates formation in the same period compared with that in the close system. However, it's easier to obtain the hydrate formation rate from gas consumption in the second method (closed system).

A fluidized bed generator, similar to the type which has been patented by Waycuilis and York (United States patent 2002, #6350928), has been used to produce CO_2 hydrate slurry continuously as shown by Zhou et al. (2015). However, the construction of such a system with a fluidized bed heat exchanger requires a large investment which is not cost-effective for industry. Simpler generators are expected to significantly improve the cost-effectiveness of these systems. In this study, a coil heat exchanger is proposed to produce CO_2 hydrate slurry. CO_2 gas is injected to the system by a long tube to mix with water (containing AFPs or not). The CO_2 saturated water solution is cooled down to form hydrates. However, this process is different from the second method mentioned by Jerbi et al. (2010). A gas volume is

maintained above the liquid and the solution is continuously sprayed into the gas phase. The apparatus of Jerbi et al. (2010) is completely filled with the solution so that there is no separate gas volume. The vessel used in this study has approximately 1.5 L filled with the gas phase. The gas volume prevents large pressure changes in the system.

It is known that thermodynamic hydrate inhibitors (THIs) including sodium chloride, methanol and glycol are the most popular hydrate inhibitors in the oil and gas industries (Yousif, 1996; Ebeltoft et al., 1997; Talaghat, 2014a,b). However, most of the thermodynamic inhibitors have to be used at high concentrations (10-50 wt%) in order to be effective which makes them less attractive (Kelland et al., 2006). Kinetic hydrate inhibitors (KHIs) are thought to be a better alternative for hydrate formation control. PVP (polyvinyl pyrrolidone), PVCap (polyvinyl caprolactam), N-Vinyl pyrrolidone-co-N-Vinyl caprolactam [poly (VP/VC)], and some lactam terpolymers are typical commercial KHIs. It has been proved that KHIs cannot avoid hydrate formation but can hinder hydrate nucleation or/and growth by adsorbing to nucleation sites or/and growth sites (Yang and Tohodi, 2011 and Fernando and Kelland, 2013). Sakaguchi et al. (2003) studied the inhibition of PVP and PVCap on structure-II hydrate crystals. They found the addition with 0.2 wt % of PVCap could strongly inhibit the hydrate growth along the interface. The addition of PVP even changes the morphology of hydrate crystals growing along the interface.

Anti-Freeze Proteins (AFPs) refer to a class of polypeptides produced by certain vertebrates, plants, fungi and bacteria that permit their survival in sub-zero environments. Shadi et al. (2008) have shown that AFPs are efficient inhibitors and comparable to the commercial polymeric inhibitors for what concerns inhibition of gas hydrate formation. Antson et al. (2001) studied the mechanism of type-III AFPs on ice growth. They confirm that type-III AFPs can make energetically favourable interactions with several ice surfaces, in such way inhibiting crystal growth. Kutschan et al. (2014) studied the dynamic mechanism of AFPs on inhibiting of ice growth and derived a correlation of the induction time as a function of concentration. Bagherzadeh et al. (2015) pointed that the ice-binding AFPs can act as a gas hydrate inhibitor. Celik et al. (2010) pointed that AFPs also modestly contribute to ice crystal superheating during melting, so that the action between AFPs and the ice surface results in a separation of the freezing point and the melting point, which is a phenomenon termed thermal hysteresis. And they mentioned the temperature change by thermal hysteresis could be about 0.5 K for moderate thermal hysteresis AFPs, such as type-III AFPs. Additionally, AFPs are

'green inhibitors' making them acceptable for both environment and human safety (Walker et al., 2015).

In this work CO_2 hydrate formation rate in a coil heat exchanger is investigated with and without the addition of AFPs. The experimental results are compared to those obtained using other additives including poly[VP/VC], which is the leading KHI on the market, and thus serve as good references when testing the KHI potential of the AFPs. A general hydrate growth equation is used to derive the change in experimental mass transfer coefficient of CO_2 from bulk liquid phase to the crystal layer. The results can be used to guide the design of a crystallizer when continuous CO_2 hydrate slurry is to be produced.

2. Experiment

2.1 Experimental apparatus

A schematic diagram of the experimental equipment is shown in Fig. 1. The equipment contains two thermostatic baths with two coil heat exchangers in each of them. The two baths are used to cool down the solution inside the coils. Two pressure sensors and two temperature sensors are located in the inlet and outlet of the cold bath respectively to measure the pressure and temperature change particularly after hydrate formation. A Coriolis flowmeter is installed to depict the flow rate and measure the density change of the solution. A speed control gear pump is used to keep the circulation of the solution. Two sight glasses are used to visualize the experiment. A storage vessel is used to keep a certain amount of slurry in the system. Gas of CO_2 can be charged through a connection with the gas bottle. Temperatures, pressures, flow rate and density are stored every 1 second by a data logger. The whole equipment has a maximum operating pressure of 40 bar.

The coil has a diameter of 120 mm (measured between the centres of the pipes). The pipe has an inner diameter of 5.6 mm. The distance between two adjacent turns is 8 mm. There are 7 turns in each coil heat exchanger. In each thermal bath, there are two coil tubes that are connected together. The total length of the coil exchanger in each bath is 4.74 m. The water filled in the system is ultra-deionized water which is used to make sure that nothing can affect the hydrate formation except the selected additive as it is well-known that electrolyte ions (like Na^+, Mg^{2+} and Cl^- etc) can inhibit the formation of gas hydrate. The experimental apparatus was filled with the ultra-deionized water and circulated to clean the system before

any experiments are processed. The total volume of the solution filled in the system is 2.5 L. It includes 1.5 L solution in the storage vessel and 1.0 L solution in the connection tubes.

The whole apparatus is installed in a stainless steel frame. The width of the apparatus is 1.5 m with a height of 1.8 m. The tubes outside of the thermostatic bath are wrapped with insulation material, therefore, the influence of the ambient temperature on the fluid is negligible in the present work.

Details of the accuracy of the instruments have been reported in Zhou et al. (2016) and are summarized in Table 1.

2.2 Experimental procedure

Experiments are firstly done with pure water and CO_2 water solution separately to validate the experimental method. Experiments were run for long periods and generally the system was maintained at constant temperature driving force for at least 30 minutes so that quasi-steady state conditions would apply. Determination of the pressure drop and heat transfer coefficient of the coil heat exchanger will be discussed below.

2.2.1 Flow characteristics

The flow phenomena in helically coiled tubes are more complex than in straight tubes due to centrifugal force effects. The transition from laminar to turbulent flow is shifted to higher Reynolds numbers (Kast, 2010):

$$Re_{crit} = 2300\left[1+8.6\left(\frac{d_i}{D_c}\right)^{0.45}\right] \tag{1}$$

For the experimental conditions, $\mathrm{Re}_{crit} = 7280$, so that for all tests the flow is laminar.

The flow in a helical coil pipe is characterised by the Dean number:

$$De = Re\sqrt{\frac{d_i}{D_c}} \tag{2}$$

The Dean number for water and CO_2 water solution is in the range 480 to 1100 with flow rate 50 ~ 110 kg h^{-1}.

The pressure drop is calculated based on Darcy–Weisbach equation:

$$\Delta P = \left(f_{str} \frac{L_{str}}{d_i} + f_c \frac{L_c}{d_i} + F_L \right) \frac{\rho \omega^2}{2} \tag{3}$$

In which, the friction factor is obtained with the Poiseuille relation for laminar flow:

$$f_{str} = \frac{64}{Re} \tag{4}$$

Frictional factor for curved tubes in relation to the friction factor for straight tubes is obtained from Naphon and Wongwises (2006):

$$\frac{f_c}{f_{str}} = 1 + 0.015 Re^{0.75} \left(\frac{d_i}{D_c} \right)^{0.4} \tag{5}$$

F_L in Eq. (3) stands for the loss caused by the sharp corners in the tubes. It was determined to be 0.9 (derived from Kast, 2010) for one turn while there are totally 5 sharp corners in the coil tube.

Fig. 2 shows a comparison of predicted and experimental pressure drop of water and CO_2 water solution at similar temperature as a function of flow rate. It indicates that the pressure drop of the water experiments can be predicted by Eq. (3) with very small errors: 1.9% and 3.7% for the flow rates 70 kg h^{-1} and 80 kg h^{-1}, respectively. Fig. 2 also shows that when CO_2 is added, so that the operating pressure rises to about 30 bar, the pressure drop increases. Notice that Fig. 2 concerns operating conditions in the aqueous solution – gas region in which there is no hydrate formation. Under these conditions not all CO_2 gas is dissolved and small CO_2 gas bubbles circulate through the system. Again the pressure drop is reasonably well predicted when a two-phase multiplier of 1.14 is applied to the pressure drop predicted for single phase liquid flow. This is indicated in the figure by the dotted line. If a Lockhart–Martinelli based two-phase pressure drop prediction method (Fsadi and Whitty, 2016; Lockhart and Martinelli, 1949) is used, such multiplier corresponds to a non-dissolved gas fraction of less than 0.2%. The under-prediction of the pressure drop at lower flows indicates that with lower velocities the gas fraction increases while with higher flows the pressure drop is over-predicted because the gas fraction reduces.

2.2.2 Heat transfer characteristics

The experimental overall heat transfer coefficient of the system is calculated based on the energy balance that results from the measured temperatures, pressures and flow rates

$$U_{\exp} = \frac{\dot{m}\Delta i - \dot{m}\frac{\Delta P}{\rho_S} - \dot{Q}_{loss}}{A\Delta T_{\ln}} \tag{6}$$

Where $\Delta T_{\ln}$ is defined as

$$\Delta T_{\ln} = \frac{(T_{inlet} - T_{bath}) - (T_{outlet} - T_{bath})}{\ln \frac{T_{inlet} - T_{bath}}{T_{outlet} - T_{bath}}} \tag{7}$$

The energy loss in Eq. 6 has been estimated to be equal to 3 W by calculating it from the length of the tube and its insulation thickness. Compared with the maximum cooling capacity, 0.3 kW, the energy loss is very small.

The general overall heat transfer coefficient without hydrates formation is calculated by Eq. (8) which is based on the internal area of the coil.

$$\frac{1}{U} = \frac{1}{h_i} + \frac{d_i \ln \frac{d_o}{d_i}}{2\lambda_w} + \frac{d_i}{d_o}\frac{1}{h_o} \tag{8}$$

In which λ_w is the thermal conductivity of stainless steel, which is taken to be 13 W m^{-1} K^{-1}.

The external heat transfer coefficient is derived from Eq. (9), which has been validated by Zhou et al. (2016).

$$h_o = 1.4\dot{Q} + 30.697 \tag{9}$$

The internal heat transfer coefficient is predicted with the correlation proposed by Xin and Ebadian (1997), which is obtained experimentally for the local heat transfer in helical pipes for laminar regime.

$$Nu = (2.153 + 0.318De^{0.643})Pr^{0.177} \tag{10}$$

For $20 < De < 2000$, $0.7 < Pr < 175$, $0.0267 < d_i/D_c < 0.0884$. Since, as discussed in section 2.2.1, the gas fraction in the solution flow is very small, this single-phase flow equation is assumed to apply for the CO_2-water solution.

Figs. 3 shows the comparison of the predicted and experimental overall heat transfer coefficient of CO_2+water solution. It indicates that Eq. (8) under predicts the experimental results, however, the average deviation is within ±10%, which is considered acceptable.

After validation, water is firstly filled into the set-up, then CO_2 is filled until a certain pressure is reached. Experiments are firstly processed without the addition of AFPs to determine the initialization point of hydrate formation and the condition for which blockage of the flow occurs. After that, the system is drained and cleaned by water before new solution with the addition of AFPs is filled. The type-III AFP used in the experiments was purchased from A/F Protein Canada Inc.

The solution with or without AFPs in the coil is cooled by the two thermostatic baths filled with tap water from 10 °C with steps of 0.5 K until there are crystals appearing in the sight glasses. Fig. 4 shows the photos taken before and after hydrates appear in the sight glass. The effective cooling capacity of each bath is 0.3 kW. The warm bath is kept at a temperature higher than the cold bath, in this way, part of the crystals formed in the cold bath will melt. In this way, solidification and melting processes of crystals allow for the fluid to remain pumpable even at higher solid concentrations.

3. Experimental Results

The experiments have been conducted by maintaining the temperature of the two thermostatic baths at a low temperature as mentioned in section 2.1. Each temperature set-point combination for the two baths is maintained for at least 30 minutes. When the temperature set points are changed the system requires some time to stabilize. This non-stationary period is not considered in the processing of the data so that steady state correlations can be used for the evaluation of the data.

3.1 Experimental results without addition of AFPs

Figs. 5-7 show the temperature and pressure change during hydrate formation period of three experimental conditions, supercooling degree, energy flow/overall heat transfer coefficient and pressure drop are also shown in these figures. The solution velocity of these three cases is 0.56 m/s, 0.68 m/s and 0.85 m/s respectively. The solution temperature is controlled by the two thermostatic baths, indicating in Fig. 5a. Fig. 5a also shows that due to the low pressure in the process, there is a gas refilling during the experiment in order to reach the hydrate formation region, which are indicated by the sudden increase before hydrates are formed (starting by the dashed red line) in Fig. 5b. While for the other two cases, gas filling is done at

least one day before, and a high pressure is maintained before experiments are done, so there is no gas refilling in the experimental day. The temperature difference between the solution and corresponding equilibrium temperature under the same pressure, which is defined as $\Delta T = T_{sol} - T_{sat}$, is used to show how far the solution deviates from equilibrium, while the equilibrium temperature is derived from Sabil (2009) as $T_{sat} = -0.0072P^2 + 0.6874P - 6.4999$. The differences between the inlet and outlet solution temperature and saturation are shown in Fig. 5c. The accuracy of these temperatures differences is ± 0.032 K. The figure indicates that the temperature difference of the inlet temperature of solution reached -1.5 K before a blockage took place (indicated by the dash-dotted line). For case 2 and case 3, the deviation from saturation is – 1.2 K and 0 K, respectively. This shows that the flow velocity influences the hydrates formation: the higher the velocity, the lower the temperature difference which leads to a blockage. Fig. 5d shows the change of sensible energy flow $\dot{Q}$ and of the overall heat transfer coefficient during the experiment. The sensible energy flow $\dot{Q}$ is derived from $\dot{Q} = \dot{m}c_p(T_{inlet} - T_{outlet})$ and excludes the latent heat of hydrate formation. Figs. 6d and 7d show that when the temperature crosses the saturation line, $\dot{Q}$ decreases, indicating that when the temperature of solution decreases below the saturation temperature, there are crystals formed, which is marked by the dash vertical line. And correspondingly, there is a pressure drop increase which is shown in Figs. 6e and 7e. However, as the crystals are formed there is no $\dot{Q}$ decrease and also no pressure drop increase in case 1 as shown in Fig. 5d and Fig. 5e respectively. It is possibly because in case 1, crystals are formed in the solution because there are a large amount of gas bubbles in the solution due to gas refilling, while for the other two cases, CO_2 gas was already dissolved into the solution. In this later case, crystals are more likely formed on the wall due to the lower temperature of the wall. Fig. 5e also shows significantly larger oscillation of the pressure drop than Fig. 6e and Fig. 7e, indicating that crystals are passing the pressure sensors. Figs. 6d and 7d also show that the $\dot{Q}$ value presents very large instantaneous changes during the formation period. This is caused by a change of set-point of thermostatic bath which induces a temperature change of the solution. Since T_{inlet} and T_{outlet} are measured at the same instant, such temperature changes lead to a jump in the $\dot{Q}$ value and as a results also of the corresponding *U* value.

From the three cases, it is concluded that hydrates start forming when the temperature of the solution is slightly below the equilibrium temperature. The second conclusion is that the

higher the solution velocity, the easier the hydrates start forming on the wall. So a lower velocity will be adopted in the next experiments. Additionally when gas is refilled during an experiment, CO_2 gas will not totally be dissolved into the solution before hydrates start forming. In the later experiments with the addition of AFPs, CO_2 gas is firstly filled to the system at least one day before the experiments are executed.

3.2 Experimental results with the addition of AFPs

As discussed above, the experiments with the addition of AFPs have been done under low velocity (0.56 m/s) of the solution and CO_2 gas has been filled in advance to the experiments. Two cases of CO_2 hydrate formation with the addition of 10 ppm AFPs are shown as Figs. 8-9. Fig. 8c indicates an inlet temperature difference of -1.9 K when the system blocks while Fig. 9c shows -1.7 K for case 2. This is caused by the larger temperature difference of the two baths. Fig. 8a shows that the temperature difference between the two baths is maintained at 1.5 K while that is 2.0 K for case 2 shown in Fig. 9a. For the two cases, the solution velocity is 0.56 m/s, and no gas has been refilled during the experiments. Notice that for the cases without addition of AFPs, shown in Figs. 5-7, the solution velocity has been varied and in the case of Fig. 5 gas has been refilled. Solution velocity has less impact than gas refilling on the results as illustrated in Figs. 5-7. For this reason the case shown in Fig. 6 is used for comparison with Figs. 8-9. Results show that the temperature difference when blockage occurs is similar for both with and without addition of AFPs, indicating a small effect of the additive. Figs. 8d and 9d show the same impact of set-point change as discussed in section 3.1.

3.3 Dissolution of CO_2 gas into the aqueous solution

Before hydrates can be formed, CO_2 gas has firstly to be dissolved into the aqueous solution. Therefore, the dissolution rate of CO_2 also influences the hydrate formation rate to some extent. Experiments for longer time have been conducted to investigate the effect of AFPs on gas dissolution.

Fig. 10 shows the experimental density change along with the system pressure for three cases: a) without the addition of AFPs; b) with 10 ppm AFPs; c) with 10 ppm AFPs and longer period. Fig. 10a shows that without AFPs, the density of solution increases when the pressure decreases because of the dissolution of CO_2 into water. The density goes to a constant value within about 33 minutes (2000 seconds); Fig. 10b shows that the density doesn't go to a constant value for a whole day experiment (7 hours); Fig. 10c shows that the solution reaches saturation only after 7 hours of operation. The effect of the addition of AFPs appears to be

limiting the first step in hydrate formation (the dissolution rate is more than 12 times slower): the CO_2 dissolution from gas to the liquid aqueous solution. This corresponds to the assumption of the simplified hydrate growth model of Skovborg and Rusmussen (1994), in which the authors assume the dissolution step to be the limiting step in hydrate formation.

4. Hydrate growth rate

4.1 Experimental hydrate growth rate

According to the discussion in section 3.1 when there is no gas refilling taking place, crystals are expected to form on the wall of the tube as schematically illustrated in Fig. 11. Fig. 11a shows the cross flow area when a crystal thickness of δ_h is attained. The flow diameter decreases from d_i to d_h. Fig. 11b shows a detail of the crystal layer. Equilibrium is assumed at the interface crystal layer / solution. The diffusion layer indicates the region through which CO_2 is transported to the interface. The crystal layer adds an extra thermal resistance. Therefore, when there is hydrate formation, the overall heat transfer coefficient would change according to the equation below

$$\frac{1}{U_h} = \frac{d_i}{d_h}\frac{1}{h_i} + \frac{d_i \ln\frac{d_o}{d_i}}{2\lambda_w} + \frac{d_i \ln\frac{d_i}{d_h}}{2\lambda_h} + \frac{d_i}{d_o}\frac{1}{h_o} \tag{11}$$

In which, the thermal conductivity of CO_2 hydrate solid, λ_h, has been taken as 0.54 W $m^{-1}K^{-1}$ for the relevant temperature range according to the value reported by Sloan and Koh (2008).

The experimental crystal thickness, $\delta=(d_i-d_h)/2$, can then be derived from Eqs. (6), (8) and (11) for the cases shown in Fig. 6 and Fig. 8. Then experimental linear growth rate of crystals can be predicted by Eq. (12).

$$v = \frac{d_i - d_h}{2\Delta t} \tag{12}$$

Figs. 12-13 show the overall heat transfer coefficient change as well as the diameter change due to the adherence of crystals to the wall for the two experiments shown in Figs. 6 and 8, respectively. Fig. 12a shows that the deviation of experimental and predicted overall heat transfer coefficient is 25% before hydrates are formed. While the deviation for Fig. 13a is larger (40%), indicating the influence of AFP on heat transfer. d_h is then derived taking the deviation of the overall heat transfer coefficient into account. Figs. 12b and 13b show the change of d_h. The instantaneous increase of the hydrate layer diameter shown in both figures

corresponds to the moments illustrates in Figs. 6 and 8 when the set-point of the thermostatic bath is changed and has no physical meanings. A decrease of 3.3 mm has been reached within 66.7 minutes before a blockage occurred for the case without additive shown in Fig. 12b. Fig. 13b indicates that a thickness of 0.8 mm has been reached and maintained for a relatively long time (66.7 minutes). This indicates the effect of the addition of AFPs.

Sabil (2009) studied the kinetic formation of CO_2 hydrate and derived the gas consumption rate. Shen et al. (2016) investigated the kinetic effect of [Py14]-Br on the formation of CO_2 hydrate. An inhibition effect has been determined with lower concentration of [Py14]-Br. The inhibition of AFP and poly (VP/VC) on methane hydrate growth has been investigated by Shadi et al. (2008). The results from these studies are used for comparison purposes.

Table 2 summarizes the influence of AFPs on CO_2 hydrate formation compared with the results from literature. It indicates that the maximum supercooling degree of CO_2 hydrate formation is only slightly influenced by the addition of AFPs. The mass growth rate, $G = vA_i\rho_h$, is derived from Eq. (12), with the hydrate density of 1036 kg m^{-3}, which is obtained from Zhou et al. (2016). Results show that the mass growth rate from this research is higher than that reported by Sabil (2009) and Shen et al. (2016). For one reason, turns in the coils make the formation easier; for another reason, the calculation is based on the whole coil, while in reality it's quite possible that hydrates form on only parts of the coil. In this study the addition of 10 ppm reduces the hydrate formation rate by approximately 35 %. With THF, the CO_2 hydrate formation rate is reduced by 27.2% according to Sabil (2009). With 0.1 wt% [Py-14]-Br, the CO_2 hydrate formation rate decreases by 17.6% according to Shen et al. (2016). Shadi et al. (2008) have investigated the impact of AFP on the methane hydrate growth rate. For pure methane/water mixture these authors found the growth rate slightly smaller than that reported for CO_2 hydrate. The growth rate is reduced by 38.2% with 70 ppm AFPs addition according to Shadi et al. (2008). The effect is similar to that with 35 ppm poly (VP/VC). Comparing the results from this research (10 ppm) and that from Shadi et al. (2008) (70 ppm), the growth rate of hydrate only slightly depends on the concentration of AFPs.

4.2 Prediction of crystal growth

Englezos et al. (1987) developed a gas hydrate growth model based on crystallization and mass transfer theories. According to their model, hydrate growth is a three-step process: 1)

gas dissolution into the liquid bulk phase; 2) diffusion of the dissolved gas to the crystal-liquid interface; 3) reaction at the interface, which is an adsorption process describing the incorporation of gas molecules into the cavities of the water structure and the subsequent stabilization of the framework of the structured water.

Skovborg and Rusmussen (1994) simplified the hydrate growth model of Englezos et al. (1987) by assuming that the transport of gas molecules from the gas phase to the liquid phase is the rate-determining step in the hydrate formation process.

In the present experiments it is clear that the dissolution of CO_2 gas into the solution is a slow process as shown in Fig. 10. Although hydrate formation can only take place after dissolution, the hydrate formation itself also requires a driving force to take place. In other words, equilibrium dissolution can be attained without the formation of crystals at all, if there is no supersaturation for hydrate formation.

The crystal layer forms along the internal tube wall due to the lower temperature than the bulk solution, and increases to a thickness of δ finally as shown in Fig. 11. After that, crystals start flowing into the solution making the solution into a slurry. However, in this work, continuous formation of crystals without blockage could not be maintained for long period (operation was limited to around 4000 s). A general crystal growth equation is applied later to derive the experimental effect of the AFP additive on the gas transportation rate in the aqueous solution.

It is expected that the diffusion rate of CO_2 gas in the solution is affected by the addition of AFPs which thereafter influence the formation of hydrates. For this reason, a model similar to the simplified model by Skovborg and Rusmussen (1994) is adopted to derive an equation describing the hydrate growth rate: Eq. (13). The equation is based on the CO_2 concentration driving force between the bulk liquid phase and the corresponding equilibrium condition at the hydrate interface. The equation is also based on the assumption that the heat transfer resistance around the particle is negligible in comparison with the mass transfer resistance.

$$G = k_l \rho_{sol} A_h (x_b^{CO_2} - x_{\text{int}}^{CO_2}) \tag{13}$$

k_l is the mass transfer coefficient of CO_2 gas from bulk liquid to the crystal interface. $x_b^{CO_2}$ is the mole fraction of CO_2 in the bulk liquid phase at the operating conditions of the heat

exchange. $x_{\text{int}}^{CO_2}$ is the mole fraction of CO_2 in the liquid-crystal layer in equilibrium with the hydrate interface temperature. A_h is the internal hydrate layer area where crystals grow on.

The concentration at the bulk liquid phase, $x_b^{CO_2}$, can be derived from the equation obtained from Duan and Sun (2003) which relates concentration, pressure and temperature.

$$x_b^{CO_2} = (0.00142T_b^{\,2} - 0.0599T_b - 0.00126T_bP - 0.000859P^2 + 0.11987P + 0.2280)/100 \quad (14)$$

The concentration of CO_2 at the liquid-crystal interface, $x_{\text{int}}^{CO_2}$, is obtained from Sabil (2009) along the clathrate equilibrium line.

$$x_{\text{int}}^{CO_2} = (0.0116T_{\text{int}}{}^{2} - 0.0091T_{\text{int}} + 1.7776)/100 \quad (15)$$

where T in Eqs. (14) and (15) is expressed in $°C$ and P is expressed in *bar*.

The interface temperature, T_{int}, is the internal wall temperature ($T_{w,i}$) in this study, which could be obtained from the energy flow balance as

$$\begin{aligned} \dot{Q} &= h_i A_i (T_{av} - T_{w,h}) \\ &= \frac{\lambda_h}{\delta_h} A_h (T_{w,h} - T_{w,i}) \\ &= \frac{\lambda_w}{\delta_w} A_w (T_{w,i} - T_{w,o}) \\ &= h_o A_o (T_{w,o} - T_{bath}) \end{aligned} \quad (16)$$

The experimental mass growth rate can be derived from Eq. (12) as $G = vA_i\rho_h$. Combining this equation with Eq. (13), the experimental mass transfer coefficient can then be obtained.

$$k_l = \frac{v\rho_h}{\rho_{sol}(x_b^{CO_2} - x_{\text{int}}^{CO_2})} \quad (17)$$

The results are shown in Table 3. It shows that the mass transfer coefficient of CO_2 in the solution is reduced by approximately 21 % when there are 10 ppm AFPs added. The results indicate that the addition of AFPs slows down the diffusion rate of CO_2 from bulk liquid phase to the crystal interface. Comparing these mass transfer rates with the dissolution rate, it is evident that the impact of the AFP additive has a significantly larger impact on the dissolution process rather than on the hydrate formation process.

Blockage is a frequently occurring problem for CO_2 hydrate production. If the addition of AFPs could help to slow down the formation rate, continuous production could be achieved. Unfortunately its effect is not sufficient to allow continuous operation. However, the results of

this research, especially how much AFPs are required to slow down the hydrate formation successfully, are important when large crystallizers are to be used for continuous production of CO_2 hydrate.

5. Conclusion

CO_2 hydrates are formed in the solution when there are large amounts of gas bubbles in the bulk solution. However, hydrates will form on the wall of the exchanger when the gas is previously dissolved in the solution.

The supercooling degree of the solution is only slightly affected by the addition of AFPs.

The addition of type-III AFPs significantly slows down the dissolution rate of gas into the solution what can be concluded from the lower solution density increase rate.

A crystal growth equation has been used to predict the effect of AFP on the diffusion rate of CO_2 from bulk to crystal layer. Results indicate that with the addition of AFPs, the hydrate formation rate is reduced by approximately 35 % what corresponds to a decrease of approximately 21 % of the mass transfer coefficient.

In summary, with a low concentration of type-III AFPs, the dissolution rate of CO_2 from gas into the solution is significantly slowed down. The mass transportation rate of CO_2 from bulk liquid to the liquid-crystal layer is also limited by the addition of AFP. However, the effect of AFP on the dissolution process is significantly larger than on the diffusion process.

ACKNOWLEDGEMENTS

The authors would like to thank KoudeGroep Delft/Wageningen for their financial support. Hongxia Zhou would like to thank Guangzhou Elites Projects of the Gangzhou Municipal Government for their financial support.

REFERENCES

Antson A.A., Smith D.J., Roper D.I., Lewis S., Caves L.S.D., Verma C.S., Buckley S.L., Lillford P.J., Hubbard R.E., 2001. Understanding the mechanism of ice binding by type III antifreeze proteins. *J. Mol. Biol.*, 305 (4), 875-889.

Ayel V., Lottin O., Peerhossaini H., 2003. Rheology, flow behaviour and heat transfer of ice slurries: a review of the state of the art. *Int. J. Refrig*., 26, 95-107.

Bagherzadeh S.A., Alavi S., Ripmeester J.A., Englezos P., 2015. Why ice binding type I antifreeze protein acts as a gas hydrate crystal inhibitor. *Phys. Chem. Chem. Phys*., 17, 9984-9990.

Bel O., Lallemand A., 1999. Study of a two phase secondary refrigerant intrinsic thermophysical properties of an ice slurry. *Int. J. Refrig*., 22, 164–74.

Celik Y., Graham L.A., Mok Y.F., Bar M., Davies P.L., Braslavsky I., 2010. Superheating of ice crystals in antifreeze protein solutions. Proc. Natl. Acad. Sci. U.S.A. 2010, 107, 5423-5428. doi:10.1073/pnas.0909456107.

Duan Z.H., Sun R. (2003). An improved model calculating CO_2 solubility in pure water and aqueous NaCl solutions from 273 to 533 K and from 0 to 2000 bar. *Chem Geol*. 193(3-4), 257-271.

Ebeltoft H., Yousif M., Soergaard E., 1997. Hydrate control during deep water drilling: Overview and new drilling fluids formulations. In proceeding of SPE Annual Technical Conference and Exhibition, San Antonio, Texas.

Edwards D.K., Denny V.E., Mills A.F., 1979. *Transfer Processes*, 2nd ed., Hemisphere, Washington, D.C.

Englezos P., 1993. Clathrate hydrates. *Ind. Eng. Chem. Res*., 32,1251–1274.

Englezos P., Kalogerakis N., Dholabhai P.D., Bishnoi P.R., 1987. Kinetics of formation of methane and ethane gas hydrates. *Chem. Eng. Sci*., 42, 2647-2658.

Fernando T., Kelland M.A., 2013. First investigation of the kinetic hydrate inhibitor performance of polymers of alkylated N-vinyl pyrrolidones. *Energy Fuels*, 27, 3730-3735.

Fournaison L., Delahaye A., Chatti I., 2004. CO_2 hydrates in refrigeration processes. *Ind. Eng. Chem. Res.*, 43, 6521-6526.

Fsadni A.M., Whitty J.P.M., 2016. A review on the two-phase pressure drop characteristics in helically coiled tubes. *Applied Thermal Engineering*, 103, 616–638.

Hammerschimidt E.G., 1934. Formation of gas hydrates in natural gas transmission lines. *Ind. Eng. Chem*., 26, 851-855.

Jager M.D., De Deugd R.M., Peters C.J., de Swaan A., Sloan E.D., 1999. Experimental determination and modeling of structure II hydrates in mixtures of methane + water + 1,4-dioxane. *Fluid Phase Equilib*., 165, 209–223.

Jerbi S., Delahaye A., Fournaison L., Haberschill P., 2010. Characterization of CO_2 hydrate formation and dissociation kinetics in a flow loop. *Int. J. Refrig*., 33, 1625-1631.

Kauffeld M., Christensen K.G., Lund S., Hansen T.M., 1999. Experience with Ice Slurry, Proc. of the 1st workshop on Ice Slurries. Yverdon-les-Bains, Switzerland, IIR, 42-73.

Kast W., 2010. Pressure drop in single phase flow in pipes. Heat Atlas VDI Second Edition 2010. Springer.

Kelland M.A., Thor S., Tomita T., Mizuta K., 2006. Studies on some alkylamide surfactant gas hydrate anti-agglomerants, *Chem. Eng. Sci*., 61, 4290-4298.

Khokhar A.A., Gudmundsson J.S., Sloan E.D., 1998. Gas storage in structure H hydrates. *Fluid Phase Equilib*., 383–392.

Kutschan B., Morawetz K., Thoms S., 2014. Dynamical mechanism of antifreeze proteins to prevent ice growth. Phys. Rev. E 90, 022711.

Lockhart R.W., Martinelli, R.C., 1949. Proposed correlation of data for isothermal two-phase, two-component flow in pipes. *Chem. Eng. Prog*., 45(1), 39-48.

Marinhas S., Delahaye A., Fournaison L., Dalmazzone D., Furst W., Petitet J-P., 2006. Modelling of the available latent heat of a CO_2 hydrate slurry in an experimental loop applied to secondary refrigeration. *Chem. Eng. and Proc.*, 45,184-192.

Matsumoto K., Namiki Y., Okada M., Kawagoe T., Nakagawa S., Kang C., 2004. Continuous ice slurry formation using a functional fluid for ice storage. *Int. J. Refrig*., 27, 73–81.

Naphon P., Wongwises S., 2006. A review of flow and heat transfer characteristics in curved tubes. *Renew. Sust. Energ. Rev*., 10, 463-390.

Ripmeester J.A., Tse J.S., Ratcliffe C.I., Powell B.M., 1987. A new clathrate hydrate structure. *Nature* 325, 135–138.

Ripmeester J.A., Ratcliffe C.I., 1990. 129Xe NMR studies of clathrate hydrate: new guest for structure II and structure H. *J. Phys. Chem*., 94, 8773–8776.

Sabil K.M., 2009. Phase behaviour, thermodynamics and kinetics of clathrate hydrate systems of carbon dioxide in presence of tetrahydrofuran and electrolytes. PhD thesis, TU Delft.

Sari O., Hu J., Eicher S., Egolf P.W., Homsy P., 2008. Thermo-physical and flow properties of CO_2 hydrate slurry. International Refrigeration and Air conditioning Conference. Purdue, US.

Sakaguchi H., Ohmura R., Mori Y., 2003. Effects of kinetic inhibitors on the formation and growth of hydrate crystals at a liquid-liquid interface. *J. Cryst. Growth*, 247, 631-641.

Shadi AI-Adel, John A.G.D, Rasha E.G., Phillip S., 2008. The effect of biological and polymeric inhibitors on methane gas hydrate growth kinetics. *Fluid Phase Equilib*., 267, 92-98.

Shen X.D., Shi L.L., Long Z., Zhou X.B., Liang D.Q., 2016. Experimental study on the kinetic effect of N-butyl-N-methylpyrrolidinium bromide on CO_2 hydrate. *J. Mol. Liq.*, 223, 672-677.

Skovborg P., Rusmussen P., 1994. A mass transport limited model for the growth of methane and the ethane gas hydrates. *Chem. Eng. Sci*., 49, 1131-1143.

Sloan E.D., 1998. Clathrate hydrates of natural gases, 2nd ed. New York: Marcel Dekker.

Sloan E.D., Koh C., 2008. Clathrate hydrates of natural gases. Taylor & Francis.

Talaghat M.R., 2014a. Enhancement of the performance of modified starch as a kinetic hydrate inhibitor in the presence of polyoxides for simple gas hydrate formation in a flow mini-loop apparatus. *J. Nat. Gas Sci. Eng*., 18, 7-12.

Talaghat M.R., 2014b. Experimental investigation of induction time for double gas hydrate formation in the simultaneous presence of the PVP and L-Tyrosine as kinetic inhibitors in a mini flow loop apparatus. *J. Nat. Gas Sci. Eng*., 19, 215-220.

Tanino M., Kozawa Y., 2001. Ice–water two-phase flow behaviour in ice heat storage systems. *Int. J. Refrig*., 24, 639–651.

Uchida T., Ebinuma T., Kawabata J., Narita, H., 1999. Microscopic observations of formation processes of clathrate-hydrate films at an interface between water and carbon dioxide. *J. Cryst. Growth*, 204, 348-356.

Walker V.K., Zeng H., Ohno H., Daraboina N., Sharifi H., Alireza Bagherzadeh S., Alavi S., Englezos P., 2015. Antifreeze protein as gas hydrate inhibitors. *Can. J. Chem.*, 93, 839-849.

Waycuilis J.J., York S.D., Production of gas hydrate slurry using a fluidized bed heat exchanger. United States patent 2002, #6350928.

Xin R. C., Ebadian M.A., 1997. The effects of Prandtl numbers on local and average convective heat transfer characteristics in helical pipes. *Int. J. Heat Fluid Flow*, 18, 482-488.

Yang D., Le L.A., Martinez R.J., Currier R., Spencer D.F., 2011. Kinetics of CO_2 hydrate formation in a continuous flow reactor. *Chem. Eng. J.*, 172:144-157.

Yang J., Tohidi B., 2011. Characterization of inhibition mechanisms of kinetic hydrate inhibitors using ultrasonic test technique. *Chem. Eng. Sci*., 66, 278-283.

Yousif M., 1996. Effect of under-inhibition with methanol and ethylene glycol on the hydrate control process. In proceedings of the Offshore Technology Conference, Houston, Texas.

Zhou H., de Sera I.E.E., Infante Ferreira C.A., 2015. Modelling and experimental validation of a fluidized bed based CO_2 hydrate cold storage system. *Appl. Energy*, 158, 433-445.

Zhou H., Vasilescu C., Infante Ferreira C.A., 2016. Heat transfer and flow characteristics during the formation of TBAB hydrate slurry in a coil heat exchanger. *Int. J. Refrig*., 64, 130-142.

Figure 1 – Schematic diagram of the experimental set-up including two thermostatic baths, two pressure sensors, two temperature sensors, a gear pump, a flowmeter, two sight glasses and a storage vessel

Figure 2 – Pressure drop during pure water and water+CO_2 experiments at similar temperature. When CO_2 is added to the water the pressure in the system rises from slightly above atmospheric pressure to around 30 bar. The lowest line shows the predicted pressure drop of water; the intermediate line shows the predicted single phase pressure drop of the solution; the top line (dotted) shows the predicted two-phase pressure drop of the solution taking the effect of non-dissolved CO_2 gas into account.

Figure 3 – Comparison of experimental and predicted overall heat transfer coefficient for water+CO_2 solution test

Figure 4 –Hydrate formation periods. Left: before hydrates appear; Center: In the middle of hydrate formation; Right: Blockage in the end of hydrate formation.

Figure 5 – Experimental results for water+CO_2 test during hydrate formation period with solution velocity of 0.56 m/s: a) temperature change, b) pressure change, c) Temperature difference change; d) energy flow/heat transfer coefficient change; e) pressure drop change.

Figure 6 – Experimental results for water+CO_2 test during hydrate formation period with solution velocity of 0.68 m/s: a) temperature change, b) pressure change, c) Temperature difference change; d) energy flow/heat transfer coefficient change; e) pressure drop change.

Figure 7 – Experimental results for water+CO_2 test during hydrate formation period with solution velocity of 0.85 m/s: a) temperature change, b) pressure change, c) Temperature difference change; d) energy flow/heat transfer coefficient change; e) pressure drop change.

Figure 8 – Experimental results for water+CO_2+AFPs test during hydrate formation period with solution velocity of 0.56 m/s case 1: a) temperature change, b) pressure change, c) Temperature difference change; d) energy flow/heat transfer coefficient change; e) pressure drop change.

Figure 9 – Experimental results for water+CO_2+AFPs test during hydrate formation period with solution velocity of 0.56 m/s case 2: a) temperature change, b) pressure change, c) Temperature difference change; d) energy flow/heat transfer coefficient change; e) pressure drop change.

Figure 10 – Solution density change along with pressure for three different cases: a) no addition of AFPs; b) with 10 ppm AFPs addition; c) with 10 ppm AFPs addition and longer period.

Figure 11 – a) Hydrates form on the internal wall of the coils; b) CO_2 transport mechanisms from gas phase to crystal layer.

Figure 12 – a) Comparison of experimental and predicted overall heat transfer coefficient for the case of no addition of AFPs shown in Fig.6. b) Diameter change during hydrate formation period.

Figure 13 – a) Comparison of experimental and predicted overall heat transfer coefficient for the case with 10 ppm AFPs shown in Fig.8. b) Diameter change during hydrate formation period.

Table 1 Summary of the uncertainties of the measured parameters.

Table 2 Hydrate formation rate summary of the experimental results and comparison with literature values.

Table 3 Comparison of mass transfer coefficient with and without the addition of AFPs.

Figure 1

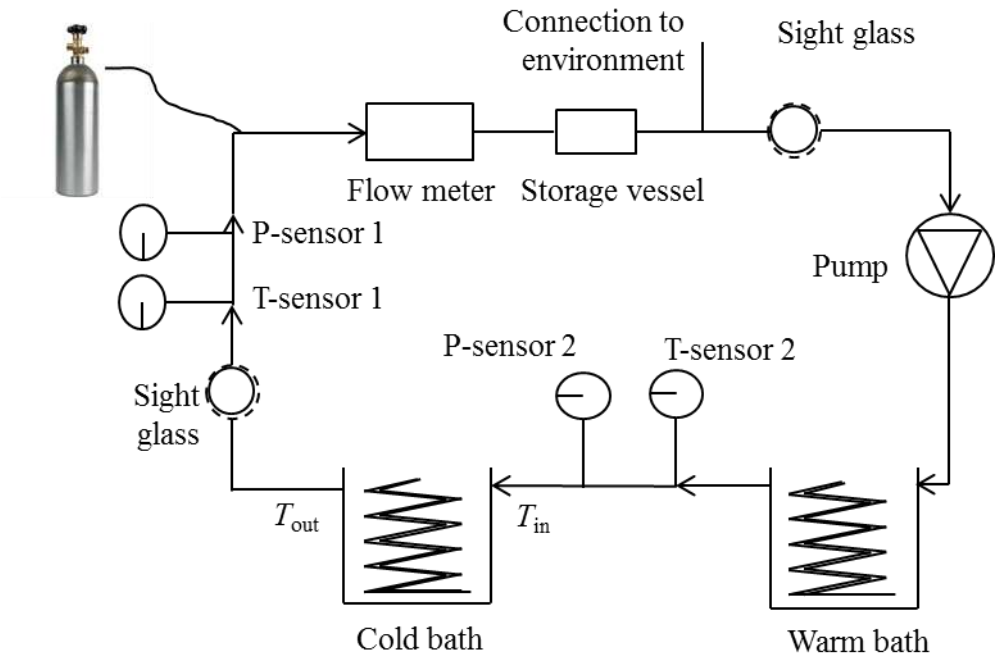
Connection to environment
Sight glass
Flow meter
Storage vessel
P-sensor 1
T-sensor 1
Pump
P-sensor 2
T-sensor 2
Sight glass
T_{out}
T_{in}
Cold bath
Warm bath

Figure 2

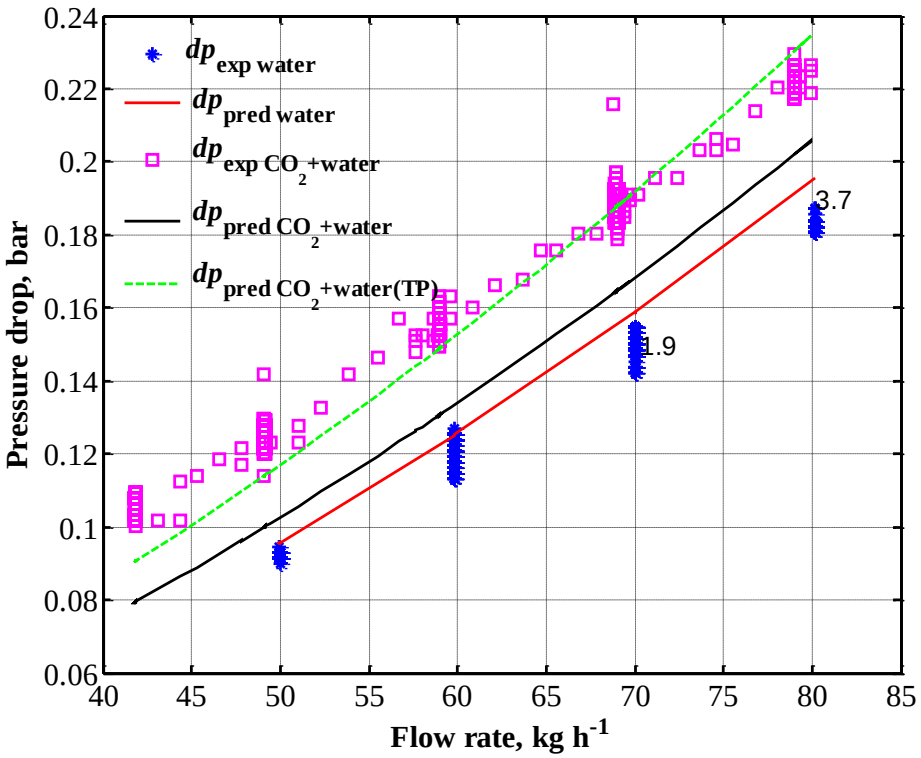
0.24
0.22
0.2
0.18
0.16
0.14
0.12
0.1
0.08
0.06
40
45
50
55
60
65
70
75
80
85
Pressure drop, bar
Flow rate, kg h-1
dpexp water
dppred water
dpexp CO2+water
dppred CO2+water
dppred CO2+water(TP)
3.7
1.9

Figure 3

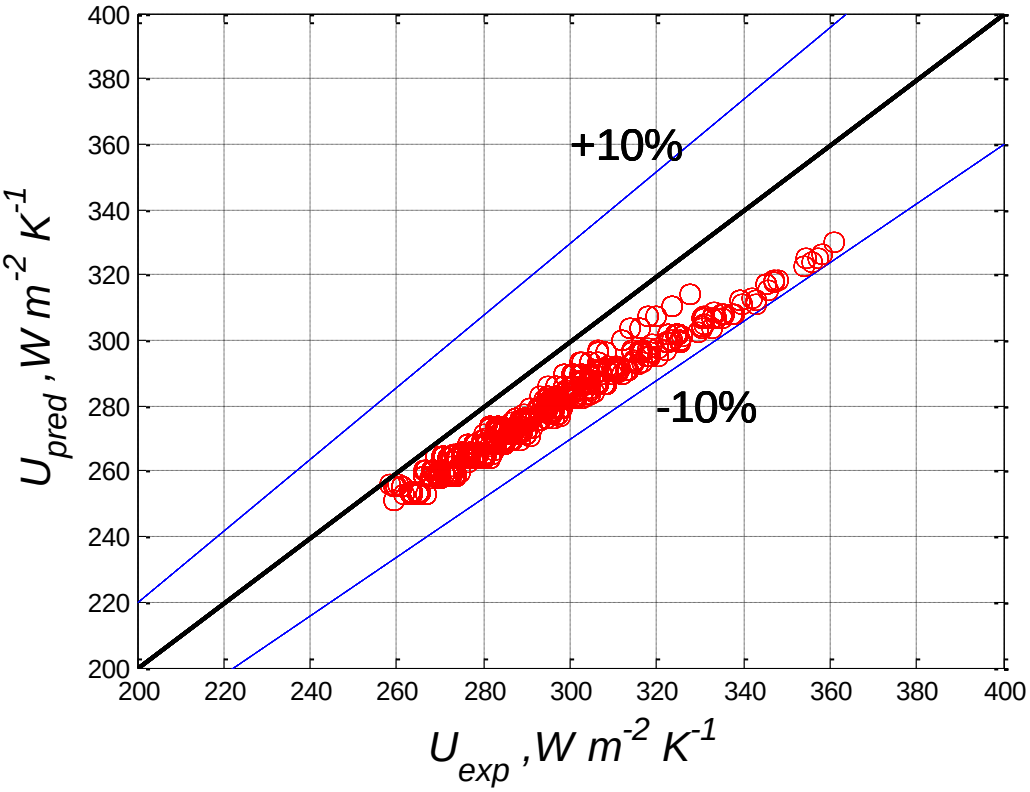
400
380
360
340
320
300
280
260
240
220
200
200
220
240
260
280
300
320
340
360
380
400
+10%
-10%
U_{pred} ,W m^{-2} K^{-1}
U_{exp} ,W m^{-2} K^{-1}

Figure 4

Figure 5—case 1: 0.56 m/s

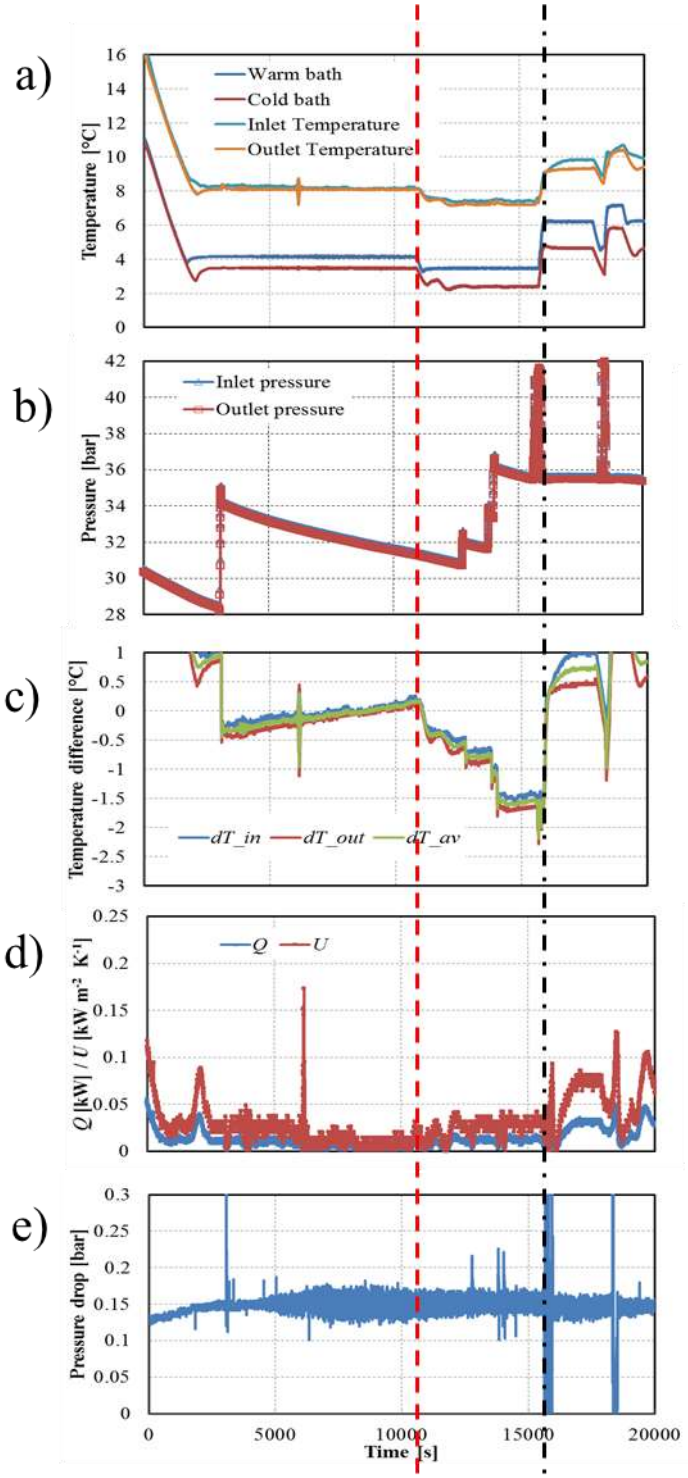

Figure 6—case 2: 0.68 m/s

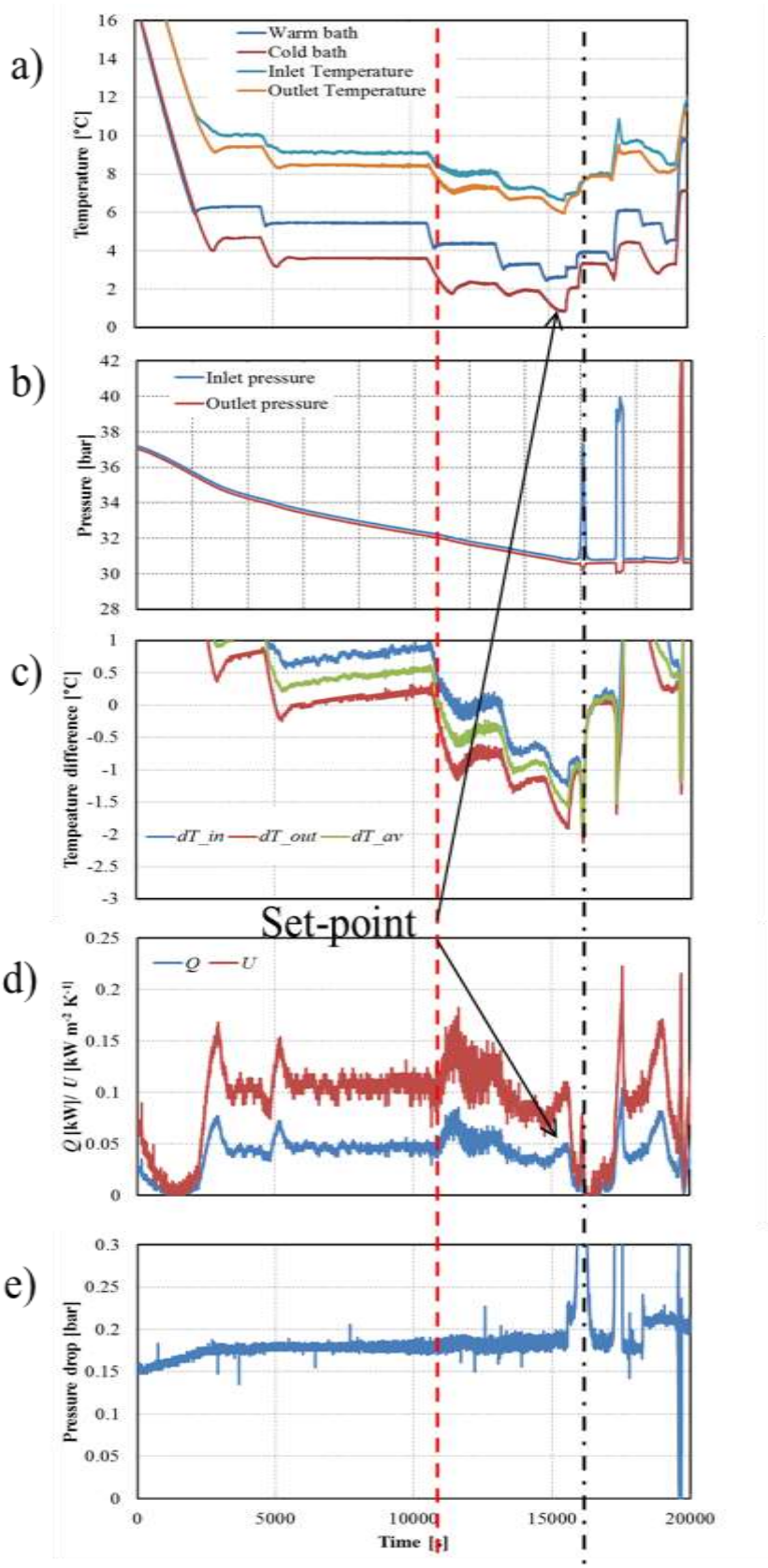

Figure 7—case 3: 0.85 m/s

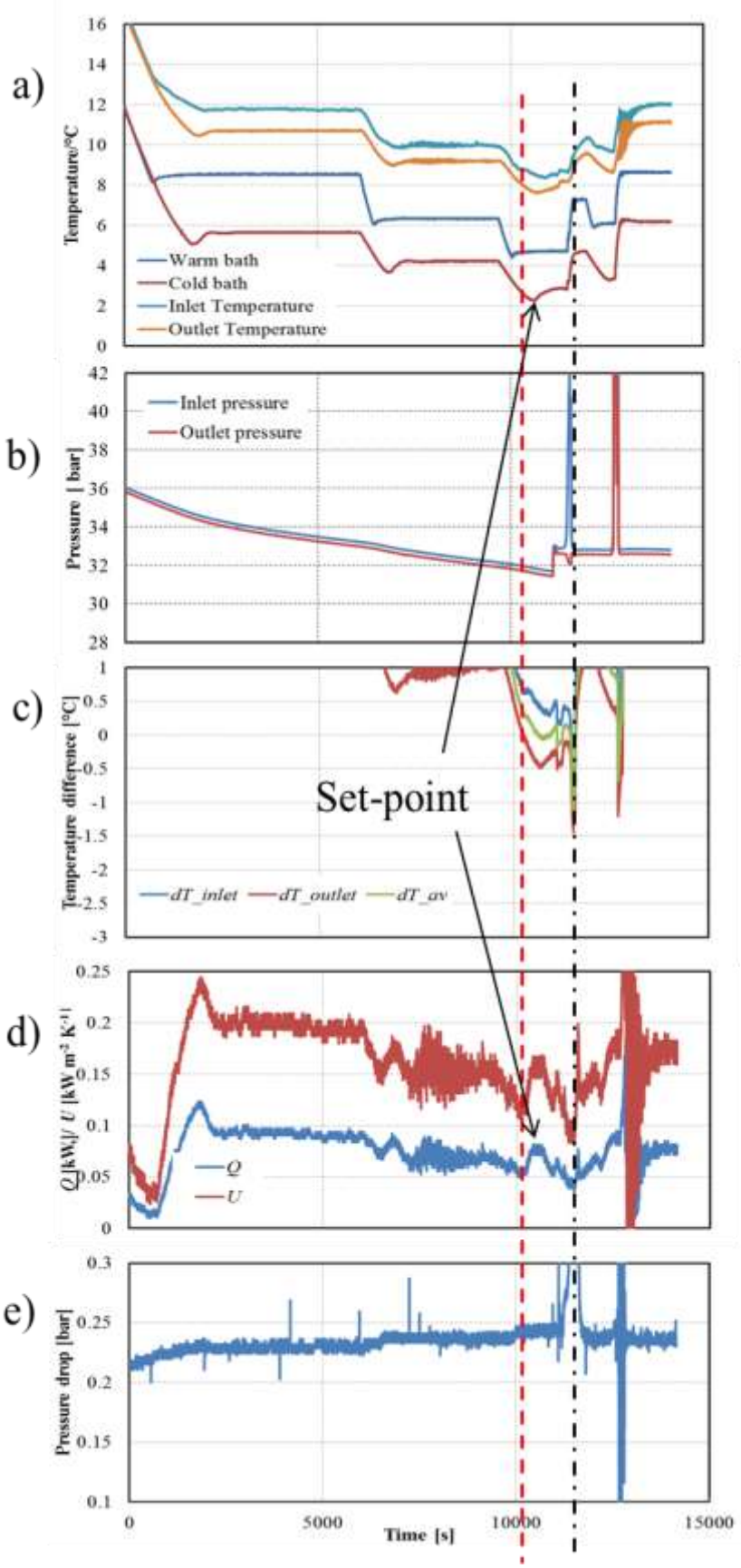

Figure 8—case 1: 0.56 m/s

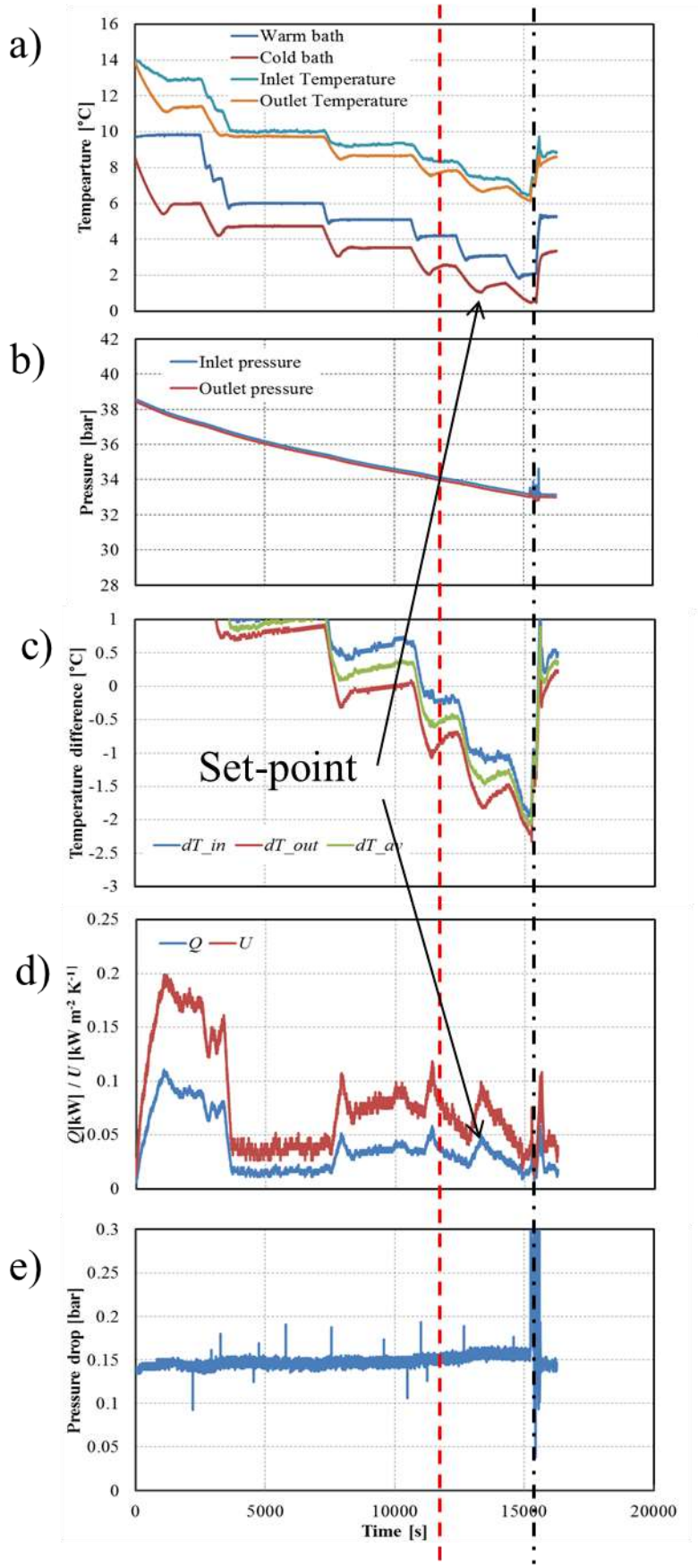

Figure 9—case 2: 0.56 m/s

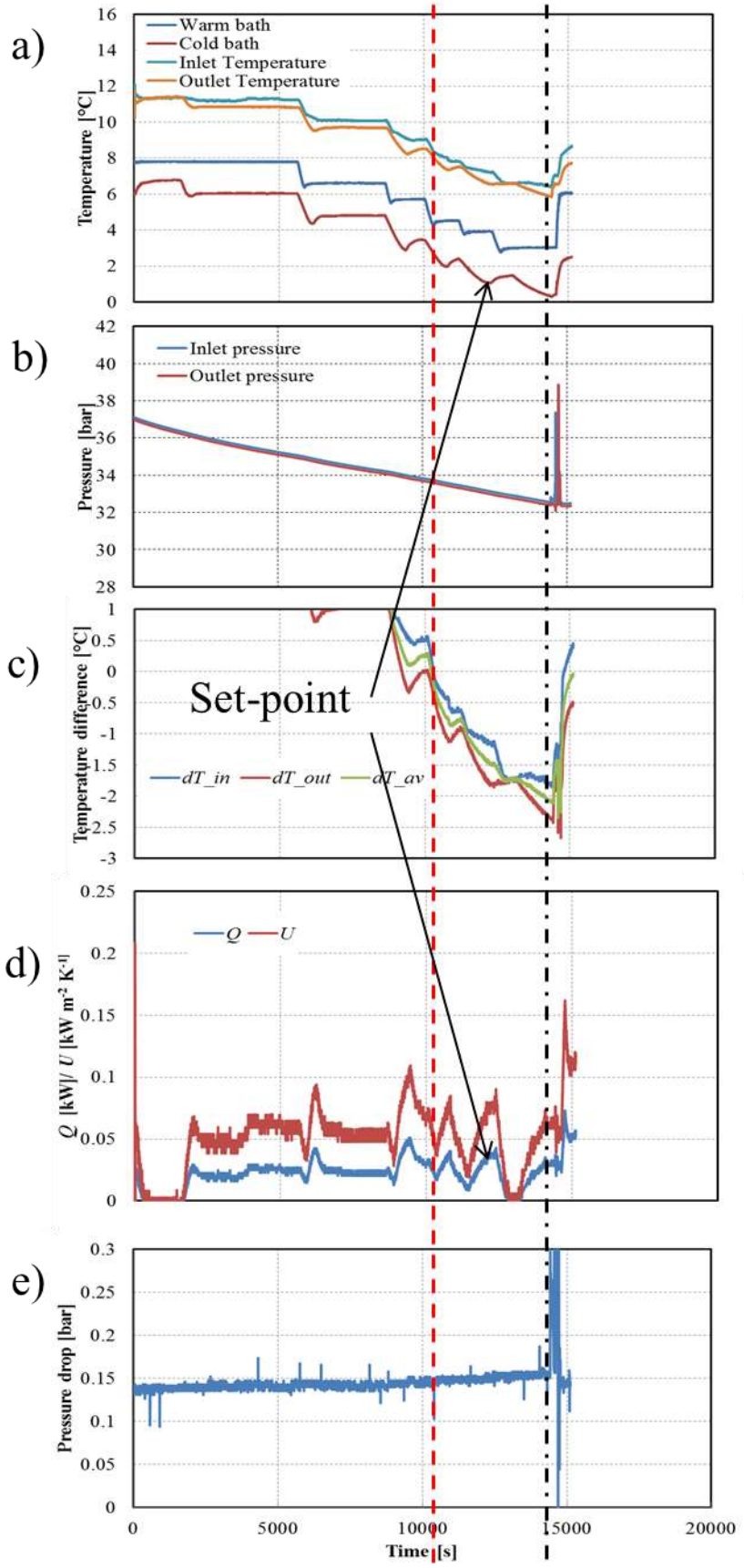

Figure 10

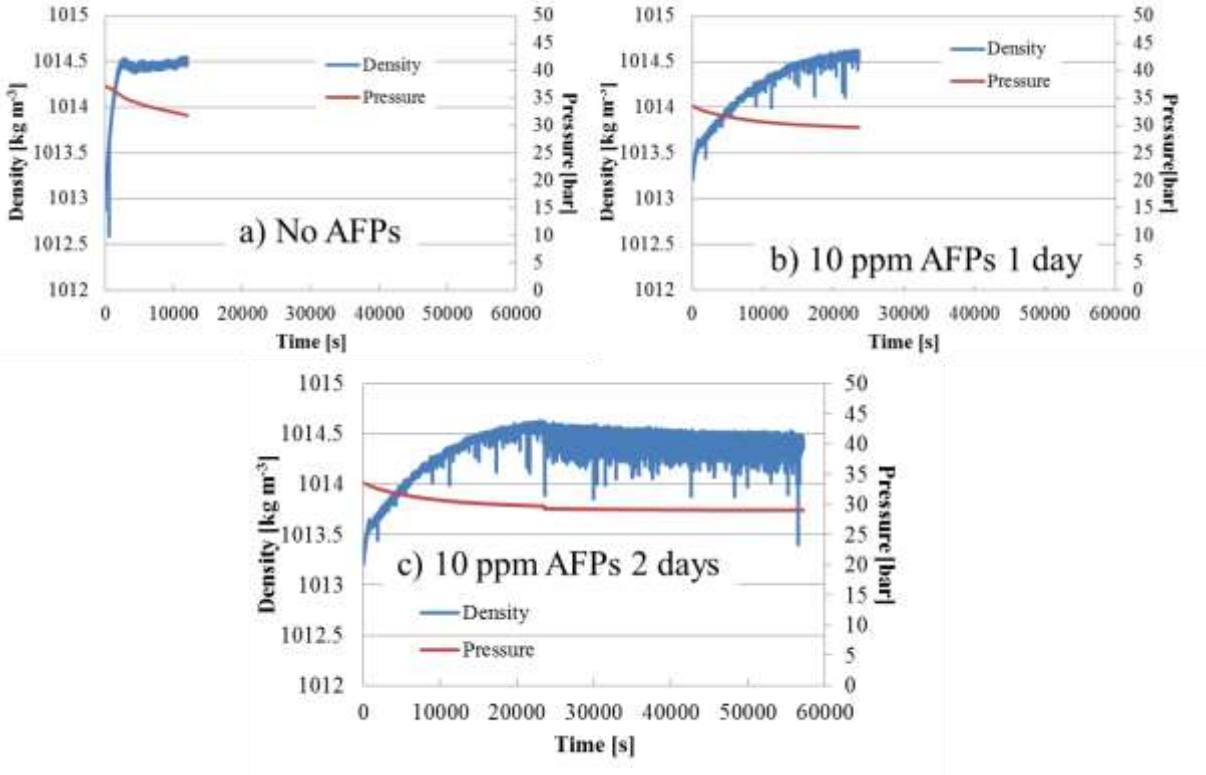
a) No AFPs
b) 10 ppm AFPs 1 day
c) 10 ppm AFPs 2 days
Density
Pressure
Density [kg m-3]
Pressure [bar]
Time [s]
1015
1014.5
1014
1013.5
1013
1012.5
1012
50
45
40
35
30
25
20
15
10
5
0
0
10000
20000
30000
40000
50000
60000

Figure 11

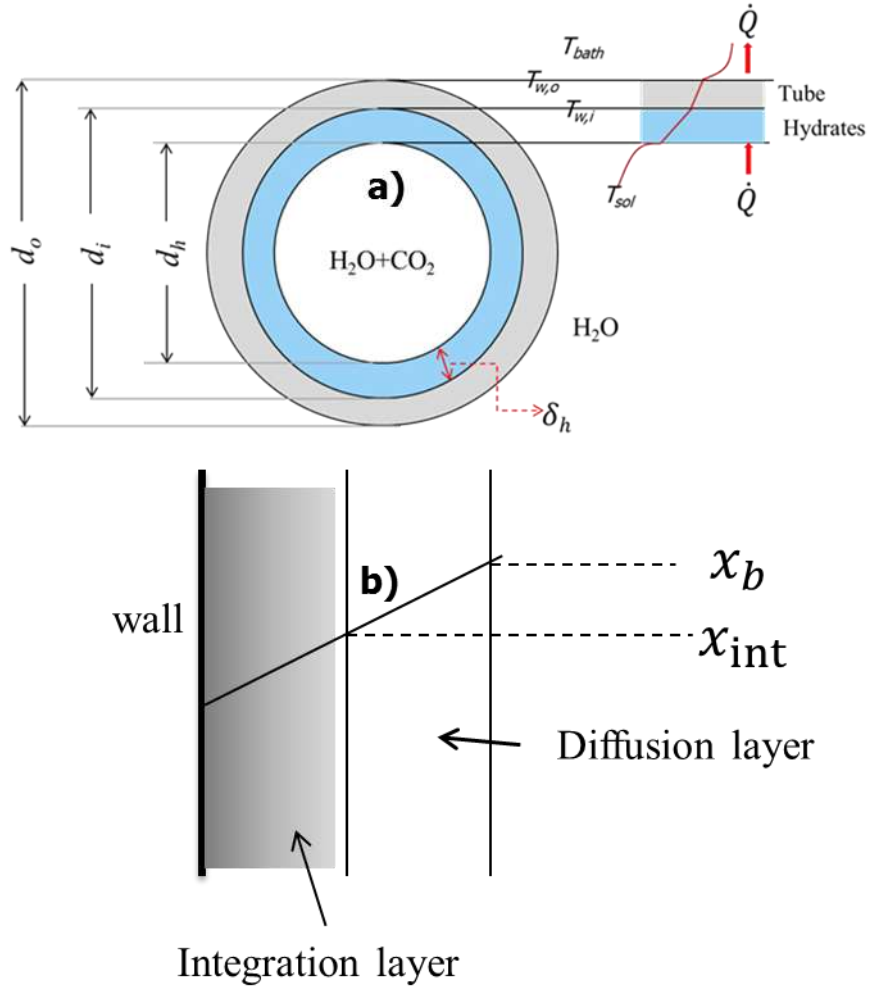
T_{bath}
$\dot{Q}$
$T_{w,o}$
$T_{w,i}$
Tube
Hydrates
a)
T_{sol}
$\dot{Q}$
d_o
d_i
d_h
H_2O+CO_2
H_2O
δ_h
wall
b)
x_b
x_{int}
Diffusion layer
Integration layer

Figure 12

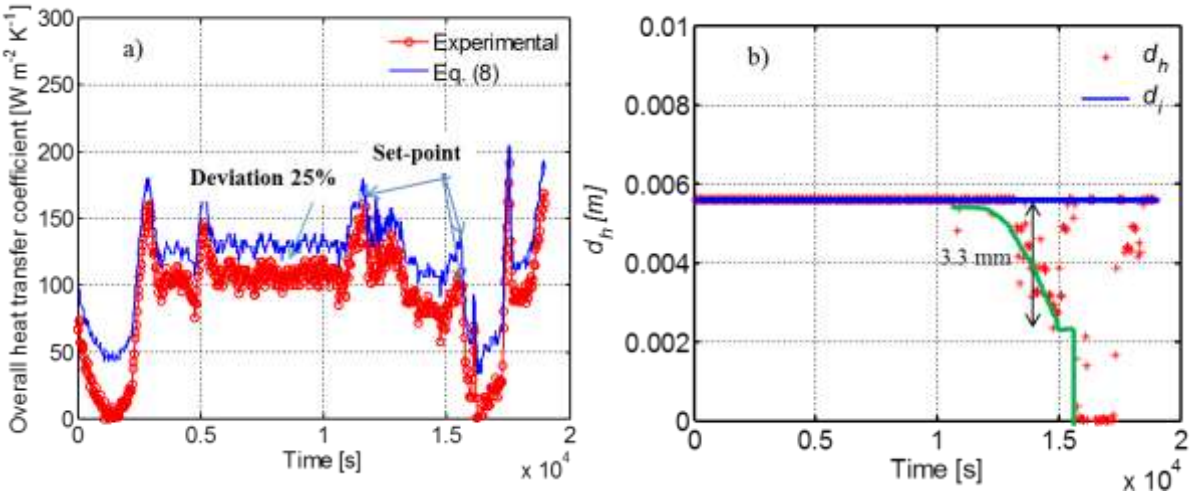
a)
Experimental
Eq. (8)
Set-point
Deviation 25%
Overall heat transfer coefficient [W m-2 K-1]
Time [s]
x 10^4
b)
dh
di
3.3 mm
dh [m]
Time [s]
x 10^4

Figure 13

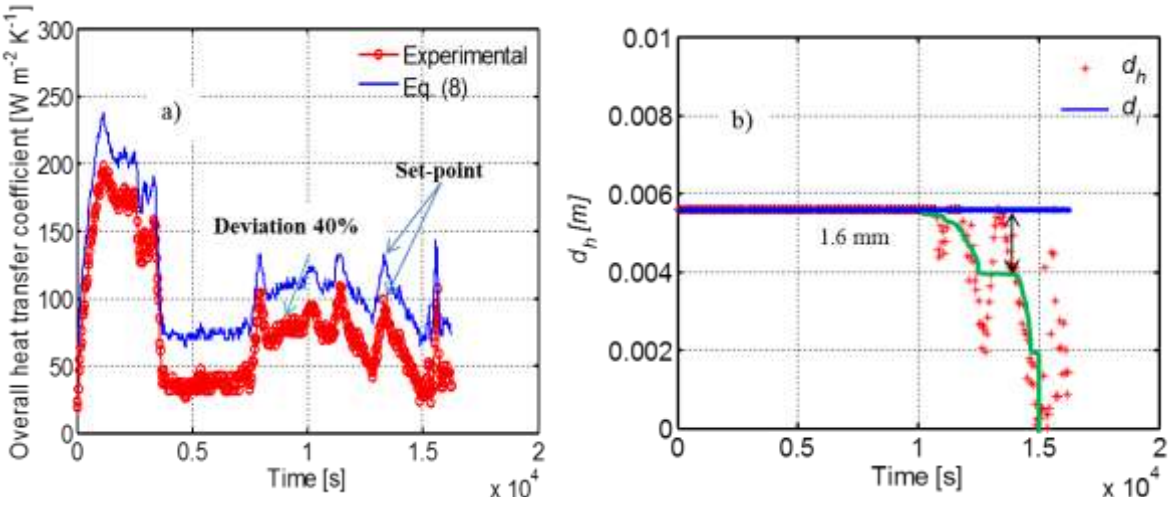
a)
Experimental
Eq. (8)
Set-point
Deviation 40%
Overall heat transfer coefficient [W m-2 K-1]
Time [s]
x 10^4
b)
dh
dl
1.6 mm
dh [m]
Time [s]
x 10^4

Table 1

Parameter	Uncertainty
Temperature / K	± 0.03
Pressure / kPa	± 1
Density / kg m^{-3}	± 0.5
Flow rate / % of full scale	± 0.15

Table 2

Additives	Max-supercooling / K	Mass Growth rate (G) / (kg h^{-1})			
		This study	Sabil (2009)	Shen et al. (2016)	Shadi et al*. (2008)
no	1.2	≈0.128	0.0125	0.017	0.011
10 ppm AFPs	1.9	≈0.083	—	—	—
THF	—	—	0.0091	—	—
0.1 wt% [Py-14]-Br	—	—	—	0.014	—
35 ppm Poly VP/VC	—	—	—	—	0.0068
70 ppm AFPs	—	—	—	—	0.0071

* This study concerns CH_4-hydrate formation with and without additives.

Table 3

x_{AFPs}	T_b	T_{int}	x_b	x_{int}	δ	v	k
—	*°C*	*°C*	*mol %*	*mol %*	*m*	$m\ s^{-1}$	$m\ s^{-1}$
0	7.68	7.48	2.488	2.358	≈0.00165	≈4.125e-7	≈3.17e-4
10 ppm	8.06	7.91	2.538	2.431	≈0.0008	≈2.67e-7	≈2.49e-4